The age–metallicity relationship in the Small Magellanic Cloud periphery

Andrés E. Piatti[1,2]⋆

[1]*Observatorio Astronómico, Universidad Nacional de Córdoba, Laprida 854, 5000 Córdoba, Argentina*
[2]*Consejo Nacional de Investigaciones Científicas y Técnicas, Av. Rivadavia 1917, C1033AAJ Buenos Aires, Argentina*

ABSTRACT

We present results from Washington CT_1 photometry for 11 star fields located in the western outskirts of the Small Magellanic Cloud (SMC), which cover angular distances to its centre from $2°$ up to $13°$ ($\approx$2.2–13.8 kpc). The colour–magnitude diagrams, cleaned from the un-avoidable Milky Way (MW) and background galaxy signatures, reveal that the most distant dominant main-sequence (MS) stellar populations from the SMC centre are located at an angular distance of $\sim$5.°7 (6.1 kpc); no sign of farther clear SMC MS is visible other than the residuals from the MW/background field contamination. The derived ages and metallicities for the dominant stellar populations of the western SMC periphery show a constant metallicity level ([Fe/H] $= -1.0$ dex) and an approximately constant age value ($\approx$7–8 Gyr). Their age–metallicity relationship (AMR) do not clearly differ from the most comprehensive AMRs derived for almost the entire SMC main body. Finally, the range of ages of the dominant stellar populations in the western SMC periphery confirms that the major stellar mass formation activity at the very early galaxy epoch peaked $\sim$7–8 Gyr ago.

Key words: techniques: photometric – galaxies: individual: SMC – Magellanic Clouds.

1 INTRODUCTION

Our knowledge about the age–metallicity relationship (AMR) of the Small Magellanic Cloud (SMC) has improved since recent – some of them still ongoing – systematic photometric studies have been carried out (e.g. Subramanian & Subramaniam 2012; Cignoni et al. 2013; Weisz et al. 2013; Rubele et al. 2015). From an over-all consensus about the formation and chemical evolution of this galaxy, some features can be highlighted: (i) an initial period of low star formation rate (SFR); (ii) an older enhanced star forma-tion process that peaked at $\sim$8 Gyr ago; (iii) another periods of intense SFR at $\sim$1.5–2.5 and 5–6 Gyr, consistent with suggestions of close encounter with the Large Magellanic Cloud (LMC) and/or the Milky Way (MW); (iv) field stars do not possess gradients in age and metallicity; (v) an AMR with a clear steady enrichment of the galactic metal content with time (older stellar populations are more metal-poor), with some variations, among others.

These main results picture the presently known assembled sce-nario for the formation and chemical evolution of the SMC main body; the farthest studied star field is located at $\sim$6.5 kpc from its centre (Noël & Gallart 2007; Carrera et al. 2008; Noël et al. 2009). However, the SMC periphery, particularly the portion towards the opposite direction to the LMC, could harbour primordial stellar pop-ulations not yet comprehensively dealt with. Nidever et al. (2011) carried out a photometric survey of the SMC periphery, from which

they extracted a modelled galactic geometry using giant star counts; no detailed study about the spatial behaviour of star field ages and metallicities were performed.

Piatti (2012a, hereafter P12) accomplished an AMR study of the SMC stellar populations from Washington CT_1 photometry of 12 star fields (36$\times$36 arcmin^2 each) getting a compromise between covering a relatively large area and reaching the oldest main-sequence turnoffs (MSTOs). He found that the field stars do not possess gradients in age and metallicity, and that stellar populations formed since $\sim$2 Gyr ago are more metal-rich than [Fe/H] ~ -0.8 dex and are confined to the innermost regions (semimajor axis $\leq$1°), along with relatively more metal-poor ([Fe/H] ~ -1.0 to -1.5 dex) and older (age $\sim$ 3–8 Gyr) field stars. He also compared the field star AMR to that of the star cluster population with ages and metal-licities in the same star field scale, and found that clusters and star fields share similar chemical evolution histories. Nevertheless, the outermost star field studied by P12 is located $\sim$4.9 kpc, so that the AMR in the SMC periphery has remained mostly unstudied.

In this paper we continue the work of P12 by studying other 11 SMC fields located in the western outskirts of the SMC. As a matter of consistency, we also analyse a Washington CT_1 data set using the same techniques. We aim at characterizing the dom-inant stellar populations distributed in that region and providing for the first time with a representative AMR. For these purposes, we structured the paper as follows: Section 2 deals with the de-scription of the photometric data sets, the reduction processes, and the various calibrations involved, including error and completeness analyses. The observed colour–magnitude diagram (CMD) features

⋆ E-mail: andres@oac.uncor.edu

Table 1. Star fields in the SMC.

Field	α_{2000} (h m s)	δ_{2000} (° ′ ″)	l (°)	b (°)	Filter (mag)	Exposure (s)	Airmass	Seeing (arcsec)
1	22 35 28	−67 06 42	320.8	−45.0	C	$1 \times 60 + 1 \times 300 + 3 \times 1080$	1.25–1.27	1.3–1.6
					R	$1 \times 10 + 1 \times 50 + 3 \times 580$	1.25–1.26	1.3–1.6
2	22 52 43	−68 05 45	318.2	−45.4	C	$1 \times 60 + 1 \times 300 + 3 \times 1080$	1.27–1.28	1.0–1.6
					R	$1 \times 10 + 1 \times 50 + 3 \times 580$	1.28–1.30	1.0–1.2
3	23 03 52	−69 18 00	316.0	−45.0	C	$1 \times 60 + 1 \times 300 + 3 \times 1080$	1.29–1.32	1.1–1.3
					R	$1 \times 10 + 1 \times 50 + 3 \times 580$	1.29	0.9–1.0
4	23 25 00	−70 24 00	313.0	−45.0	C	$1 \times 60 + 1 \times 300 + 3 \times 1080$	1.40–1.52	1.3–1.5
					R	2×580	1.54–1.56	1.2
5	23 32 08	−70 41 27	312.1	−45.0	C	$1 \times 60 + 3 \times 1080$	1.38–1.46	1.4–1.6
					R	$1 \times 10 + 3 \times 580$	1.32	1.1–1.3
6	0 04 31	−66 22 33	310.2	−50.1	C	$1 \times 60 + 1 \times 300 + 3 \times 1080$	1.24–1.25	1.3–1.6
					R	$1 \times 10 + 1 \times 50 + 3 \times 580$	1.24–1.26	1.0–1.2
7	23 55 20	−69 28 35	310.1	−46.9	C	$1 \times 60 + 1 \times 300 + 3 \times 1080$	1.43–1.60	1.0–1.2
					R	$1 \times 10 + 1 \times 50 + 3 \times 580$	1.40–1.45	1.1–1.3
8	23 55 00	−71 20 00	309.1	−45.1	C	$1 \times 60 + 1 \times 300 + 3 \times 1080$	1.33–1.34	1.2–1.3
					R	$1 \times 10 + 1 \times 50 + 3 \times 580$	1.35–1.38	0.9–1.0
9	0 04 02	−70 59 48	308.4	−45.6	C	$1 \times 60 + 1 \times 300 + 3 \times 1080$	1.34–1.38	1.0–1.3
					R	$1 \times 10 + 1 \times 50 + 3 \times 580$	1.32–1.33	1.2–1.4
10	23 41 16	−73 08 22	309.8	−43.0	C	$1 \times 60 + 1 \times 300 + 3 \times 1080$	1.37–1.41	1.5–1.7
					R	$1 \times 10 + 1 \times 50 + 2 \times 580$	1.37	1.0
11	0 43 21	−70 54 00	303.9	−46.2	C	$1 \times 60 + 1 \times 300 + 4 \times 1080$	1.32–1.34	1.4–1.6
					R	$1 \times 10 + 1 \times 50 + 3 \times 580$	1.40–1.45	1.1–1.3

as well as the cleaning procedures for decontaminating them from the MW/background galaxy signatures are described in Section 3. In Section 4, we estimate the ages and metallicities of the dominant stellar populations in each SMC field, and discuss their AMR to the light of the most comprehensively known SMC AMRs. Concluding remarks are given in Section 5.

2 DATA HANDLING

In our previous series of studies of SMC clusters and star fields (see e.g. Piatti 2011c; P12), we used the Washington CT_1 photometric system (Canterna 1976) from which ages and metallicities for stellar populations older than ∼1 Gyr can be estimated (Piatti & Perren 2015, and references therein). For these reasons, and in order to keep consistency with our previous studies, we performed a search within the National Optical Astronomy Observatory (NOAO) Science Data Management (SDM) Archives[1] seeking for Washington photometric data towards the SMC periphery. As a result, we found images obtained at the Cerro-Tololo Inter-American Observatory (CTIO) 4 m Blanco telescope with the MOSAIC II camera (36×36 arcmin^2 field with a 8k×8k CCD detector array, scale 0.274 arcsec pixel^{-1}) covering 11 fields in the SMC outskirts for a total area of ∼4.0 deg^2 (programme CTIO 2006B-0013, PI: Saha). The log of the observations is presented in Table 1, where the main astrometric, photometric, and observational information is summarized. Note that the data set includes the filter R which is a more efficient substitute of the T_1 filter (Geisler 1996), but our final standard magnitude is the Washington T_1 mag. Fig. 1 depicts the spatial distribution of the SMC fields, where we included those in P12 for comparison purposes. The maximum angular distance probed from the centre of the SMC is ∼13°.0.

The Washington CT_1 photometric data set used in this work were obtained from a comprehensive process that involved the reduction
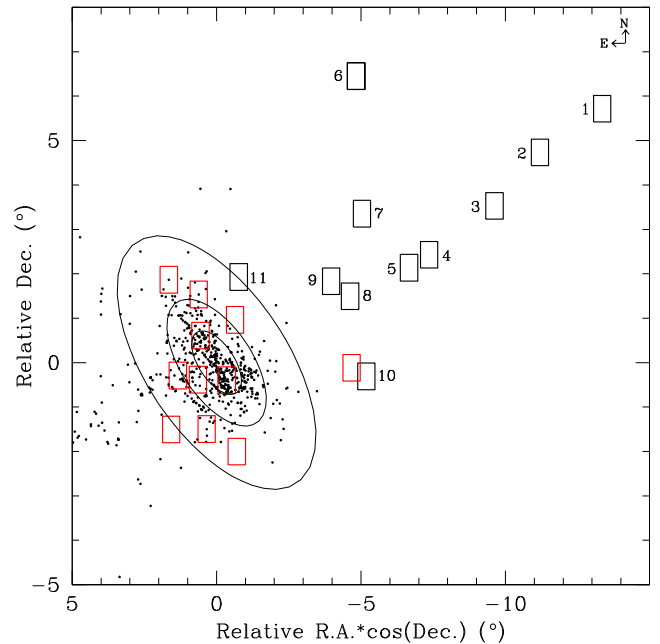
Figure 1. Spatial distribution of the presently studied SMC star fields (thick black boxes) and of those in P12 (thick red boxes). Star clusters catalogued by Bica et al. (2008) are also drawn (dots) for comparison purposes. Ellipses with semimajor axes of 1°, 2°, and 4° are overplotted .

of the raw images, the determination of the instrumental photometric magnitudes, and the standardization of the photometry. We have already described in detail such steps not only in the works cited above, but also in Piatti (2011a, 2011b, 2011c, 2012b), Piatti & Bica (2012), Piatti, Geisler & Mateluna (2012), and Maia, Piatti & Santos (2014). For this reason, we summarize here some specific issues in order to provide the reader with an overview of the photometry quality. The data reduction followed the procedures documented by

[1] http://www.noao.edu/sdm/archives.php.

the NOAO Deep Wide Field Survey team (Jannuzi, Claver & Valdes 2003) and utilized the MSCRED package in IRAF.[2] We performed overscan, trimming, and cross-talk corrections, bias subtraction, flattened all data images, etc., once the calibration frames (zeros, sky-, and dome- flats, etc.) were properly combined. For each image we obtained an updated world coordinate system (WCS) data base with an rms error in right ascension and declination smaller than 0.4 arcsec, by using ∼500 stars catalogued by the USNO.[3]

We also retrieved MOSAIC II and CTIO 0.9 m CFCCD images of the standard fields SA 92 and SA 98 observed as part of the same programme. The reduction of the MOSAIC II data set was performed following the steps as for the SMC fields. These standard fields contain between 8 and 14 standard stars each (Geisler 1996) and series of eight observations were carried out by dithering the images, so that most of the standard stars were distributed on each of the MOSAIC II's eight chips. This observing procedure was repeated for different airmasses. The images from the CTIO 0.9 m telescope were taken with the Tektronix 2k#3 CCD, using quad-amp readout. The scale on the chip is 0.4 arcsec pixel^{-1} yielding an area covered by a frame of 13.5×13.5 arcmin^2. The integrated IRAF-Arcon 3.3 interface for direct imaging was employed as the data acquisition system. The data were processed using the QUADPROC package in IRAF. After applying the overscan-bias subtraction for the four amplifiers independently, we carried out flat-field corrections using a combined sky-flat frame, which was previously checked for a non-uniform illumination pattern with the averaged dome-flat frame.

We derived nearly 80 independent magnitude measures of standard stars per filter for each night using the APPHOT task within IRAF, in order to secure the transformation from the instrumental to the Washington CT_1 standard system. The relationships between instrumental and standard magnitudes were obtained by fitting the equations:

$$c = a_1 + T_1 + (C - T_1) + a_2 \times X_C + a_3 \times (C - T_1), \quad (1)$$

$$r = b_1 + T_1 + b_2 \times X_R + b_3 \times (C - T_1), \quad (2)$$

where a_i and b_i ($i = 1$, 2, and 3) are the fitted coefficients, and X represents the effective airmass. Capital and lowercase letters represent standard and instrumental magnitudes, respectively. We solved the transformation equations with the FITPARAMS task in IRAF for each night, and substituted the derived mean zero-point and colour term ($a_3 = -0.090$, $b_3 = -0.020$) values for each observing run into the above equations and solved for the airmass coefficient for each night. Typical values of a_2 and b_2 were 0.305 and 0.095 mag airmass^{-1}, respectively. The nightly rms errors from the transformation to the standard system were 0.021 and 0.017 mag for C and T_1, respectively, indicating the nights were of excellent photometric quality.

The stellar photometry was performed using the star-finding and point-spread-function (PSF) fitting routines in the DAOPHOT/ALLSTAR suite of programs (Stetson, Davis & Crabtree 1990). We measured magnitudes on the single image created by joining all eight chips together using the updated WCS. This allowed us to use a unique reference coordinate system for each SMC field. For each Mosaic image, a quadratically varying PSF was derived by fitting ∼1000 stars (nearly 110–130 stars per chip), once the neighbours were eliminated using a preliminary PSF derived from the brightest, least contaminated ∼250 stars (nearly 30–40 stars per chip). Both groups of PSF stars were interactively selected. We then used the ALLSTAR program to apply the resulting PSF to the identified stellar objects and to create a subtracted image which was used to find and measure magnitudes of additional fainter stars. This procedure was repeated three times for each frame. We computed aperture corrections from the comparison of PSF and aperture magnitudes by using the neighbour-subtracted PSF star sample. After deriving the photometry for all detected objects in the C and T_1 filters, a cut was made on the basis of the parameters returned by DAOPHOT. Only objects with $\chi < 2$, photometric error less than 2σ above the mean error at a given magnitude, and $|\text{SHARP}| < 0.5$ were kept in each filter, and then the remaining objects in the C and T_1 lists matched with a tolerance of 1 pixel.

Finally, we standardized the resulting instrumental magnitudes and combined all the independent measurements using the stand-alone DAOMATCH and DAOMASTER programs.[4] The final information for each field consists of a running number per star, its right ascension and declination coordinates, the averaged T_1 magnitude and $C - T_1$ colour, the standard errors $\sigma(T_1)$ and $\sigma(C - T_1)$ and the number of measurements in the C and T_1 filters. Whenever a star does have only one measure of C and T_1 magnitudes, the errors provided by the DAOPHOT/ALLSTAR routines were listed. Table 2 gives this information for Field 1. Only a portion of this table is shown here for guidance regarding its form and content. The whole content of Table 2, as well as the final information for the remaining fields, is available in the online version of the journal.

As is well known, photometric errors, crowding effects, and the detection limit of the images cause incompleteness and therefore result in the increasing loss of stars at fainter magnitudes. Commonly, artificial star tests on the deepest images are performed in order to derive the completeness level at different magnitudes. We used the stand-alone ADDSTAR program in the DAOPHOT package (Stetson et al. 1990) to add synthetic stars, generated at random with respect to position and magnitude, to each deepest image in order to derive its completeness level. We added a number of stars equivalent to ∼5 per cent of the measured stars in order to avoid in the synthetic images significantly more crowding than in the original images. On the other hand, to avoid small number statistics in the artificial-star analysis, we created five different images for each original one. We used the option of entering the number of photons per ADU in order to properly add the Poisson noise to the star images.

We then repeated the same steps to obtain the photometry of the synthetic images as described above, i.e. performing three passes with the DAOPHOT/ALLSTAR routines. The star-finding efficiency was estimated by comparing the output and the input data for these stars using the DAOMATCH and DAOMASTER tasks. We illustrate in Fig. 2 the resultant completeness fractions in the T_1 versus $C - T_1$ CMD for the most populated field in our sample (Field 11). Fig. 2 shows that the 50 per cent completeness level is located at $C \sim 23.75$ mag and $T_1 \sim 24.25$ mag; for less crowded fields this completeness level reaches down to ∼0.75–1.00 mag fainter, depending on the crowding. Note that according to the theoretical isochrones computed by Bressan et al. (2012) and considering the SMC distance modulus $(m - M)_o = 18.96$ (de Grijs & Bono 2015), a 13 Gyr old
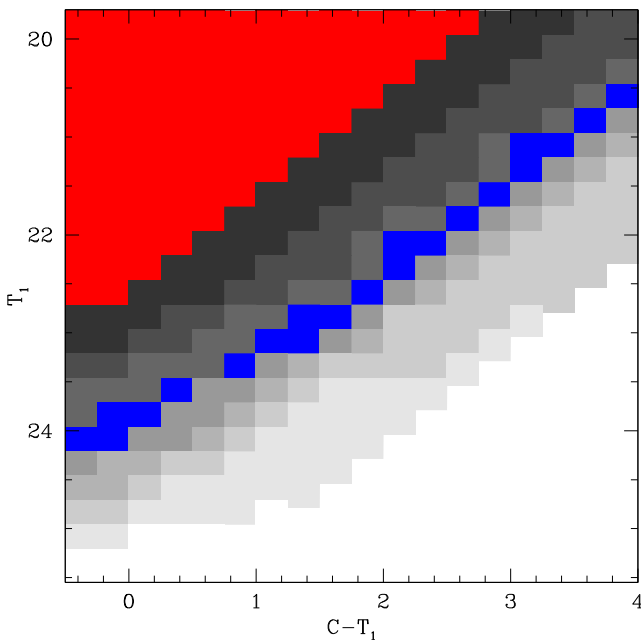
---

[4] Provided kindly by Peter Stetson.

Table 2. CT_1 data of stars in Field 1. The complete table is available online as Supporting Information.

Star	α_{2000} (hms)	δ_{2000} (° ′ ″)	T_1 (mag)	$\sigma(T_1)$ (mag)	$C - T_1$ (mag)	$\sigma(C - T_1)$ (mag)	n
–	–	–	–	–	–	–	–
124	22:32:29.120	−67:23:03.58	18.130	0.003	1.037	0.006	5
125	22:33:54.381	−67:23:13.03	15.868	0.003	1.338	0.004	5
126	22:33:32.216	−67:23:10.47	19.910	0.007	2.719	0.073	4
–	–	–	–	–	–	–	–

Figure 2. Grey-scale completeness fraction for the most crowded field in our sample (Field 11). The higher the completeness fraction, the darker the CMD. Red and blue regions represent the 100 per cent and 50 per cent completeness levels, respectively.

stellar population ([Fe/H] $\approx$ −1.3 dex) should have its MSTO at $T_1 \approx 22.5$ mag. Therefore, our photometry reaches the 50 per cent completeness level 2–3 mag below the oldest known SMC MSTOs (Carrera et al. 2008; Noël et al. 2009).

3 GLOBAL PROPERTIES OF THE CMDS

In Fig. 3 we plot the CMDs for all measured stars in each SMC field. We measured from ~11 up to 76 000 stars from the outermost to the innermost fields, with an average of ~33 000 stars, thus yielding a CT_1 photometric data base of ~175 000 stars. The CMDs present a strong signature of the foreground/background fields which blurs the SMC outskirts main features. Nevertheless, it can be seen an old main-sequence (MS) population in Field 7 ($C - T_1 \approx 0.8$, $T_1 \sim 22$–23), and increasing younger populations (brighter T_1 MSTOs) for inner SMC fields. Thus, the series of panels depicted in Fig. 3 shows the age transition of the stellar populations in the outermost SMC regions. At the right margin of each panel, we show the behaviour of the errors $\sigma(T_1)$ and $\sigma(C - T_1)$. As can be seen, it would seem that a relatively small dispersion accompanies the intrinsic features along almost ~9 mag.

3.1 Cleaning the CMDs

In order to disentangle the MW/background signature in the peripheral SMC CMDs, we applied a procedure primarily developed by Piatti & Bica (2012, see fig. 12) to clean star cluster CMDs from field star contamination (see e.g. Piatti 2014; Piatti et al. 2014b, 2015). Comparisons of field and cluster CMDs have long been done by comparing the numbers of stars counted in boxes distributed in a similar manner throughout both CMDs. However, since some parts of the CMD are more densely populated than others, counting the numbers of stars within boxes of a fixed size is not universally efficient. For instance, to deal with stochastic effects at relatively bright magnitudes (e.g. fluctuations in the numbers of bright stars), larger boxes are required, while populous CMD regions can be characterized using smaller boxes. Thus, use of boxes of different sizes distributed in the same manner throughout both CMDs leads to a more meaningful comparison of the numbers of stars in different CMD regions.

For our purposes, we adopted Field 1 as the MW/background field CMD, which is located ~3–4° farther than the SMC boundary delimited by Nidever et al. (2011). We also assumed that the MW/background field is uniform in terms of luminosity function, colour distribution, and stellar density across the surveyed region (Balbinot et al. 2015). Note that the 11 SMC fields are projected over a relatively small MW area of ~16×7 deg². We checked this assumption for the MW by building a series of synthetic CMDs using the Besançon galactic model (Robin et al. 2003). Note that MW models can only include MW stars and not distant unresolved galaxies, which occur in significant numbers at faint magnitudes. The typical number of generated stars represent ~50 per cent of the stars measured in Field 1. Consequently, the present cleaning procedure allows us to recognize the location of the bulk of the SMC population, while more sophisticated approaches might provide more quantitative outcomes (e.g. Roderick et al. 2015).

We then compare the MW/background CMD – previously corrected by the difference in reddening (see column 2 of Table 3) and in completeness effects – to each one of the SMC CMDs and subtract from the latter a representative MW/background CMD in terms of stellar density, luminosity function, and colour distribution. The representative MW/background CMD was built from scanning the observed MW/background CMD using boxes that vary in size, thus achieving a better MW/background representation than counting the number of stars in boxes fixed in size. Then, the stars in the SMC CMDs that fall within the defined boxes and closest to the representative positions were eliminated.

The method allows that boxes vary in magnitude and colour separately according to the free path between stars in the CMD, so that they result bigger in CMD regions with a small number of stars, and vice versa. The free path is defined as $\Delta(\text{colour})^2 + \Delta(\text{magnitude})^2 = (\text{free path})^2$, where $\Delta(\text{colour})$ and $\Delta(\text{magnitude})$ are the distances from the considered star to the closest one in
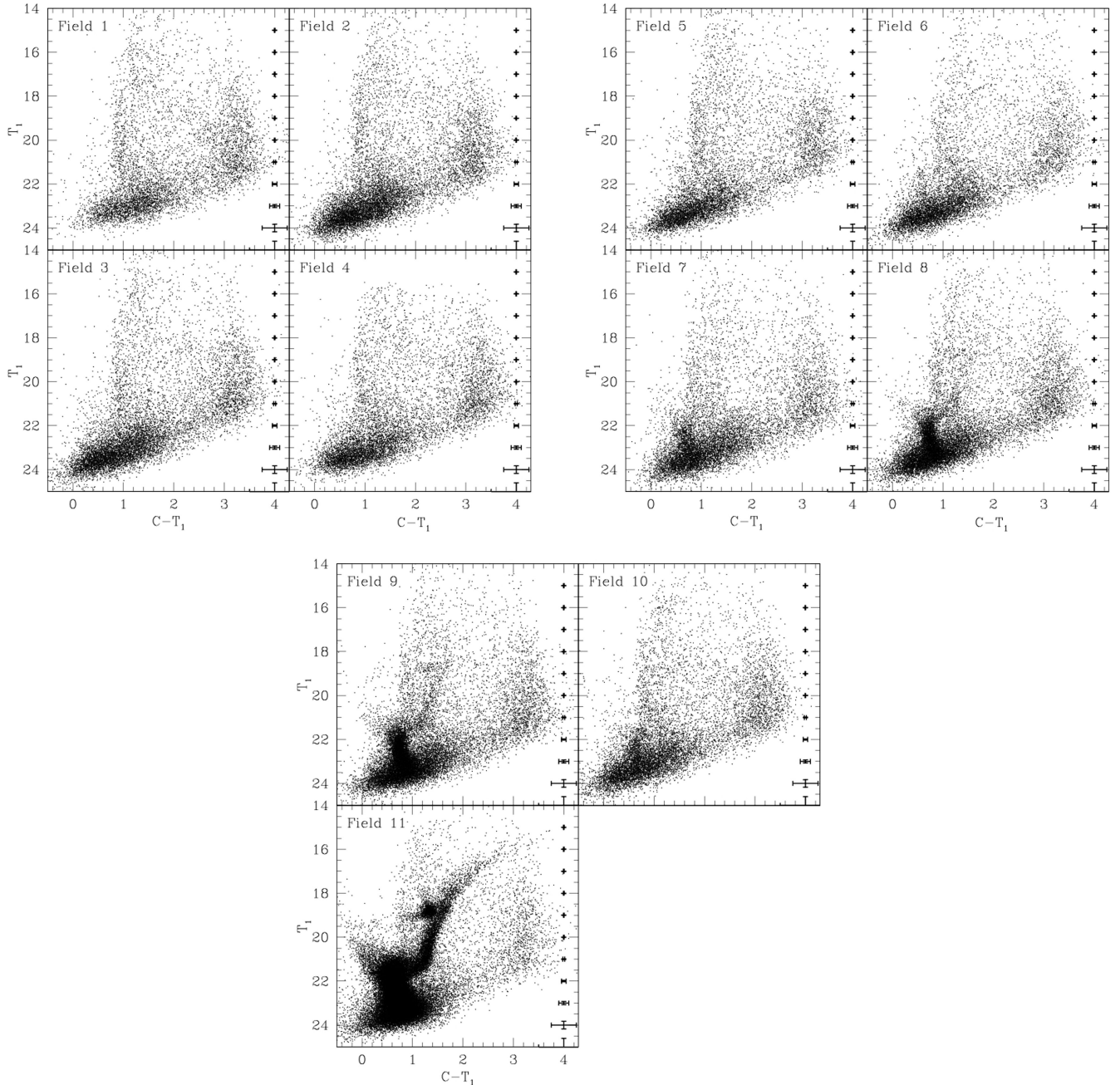
Figure 3. CMDs of stars measured in SMC fields.

abscissa and ordinate in the MW/background CMD. In practice, an initial reasonably large box with a dimension of (Δ(colour), Δ(magnitude) = (0.5, 1.0)) is centred on each single star in the MW/background CMD. Then, the method subsequently reduces the box sizes until they reach the stars closest in magnitude and colour, separately, so that the resulting closest magnitude and colour will be used to define the free path of the considered star. The task is repeated for every star in the MW/background CMD. Therefore, each star in the MW/background CMD has associated a different box.

These boxes are then superimposed to the SMC CMDs, and the stars closest to their centres are eliminated. In this sense, the box

sizes depend not only on the stellar density of the MW/background field (the denser a field the more stars in the MW CMD), but also on the magnitude and colour distributions of those stars in the MW/background CMD, making some parts of the MW/background CMD more populated than others. For instance, relatively bright field red giants with small photometric errors usually appear relatively isolated at the top-right zone of the CMD, while faint MS stars are more numerous at the bottom part of the CMD. For this reason, bigger boxes are required to satisfactorily subtract stars from the SMC CMD regions where there are a small number of MW/background stars, while smaller boxes are necessary for those CMD regions more populated by MW/background stars.

Table 3. Fundamental properties of studied SMC fields.

Field	$E(B-V)$ (mag)	Angular distance (deg)	Age (Gyr)	[Fe/H] (dex)
1	0.024	12.8	–	–
2	0.026	10.9	–	–
3	0.029	9.4	–	–
4	0.037	7.3	–	–
5	0.034	6.6	–	–
6	0.018	7.7	–	–
7	0.027	5.7	8 ± 2	-1.0 ± 0.3
8	0.029	4.7	8 ± 2	-1.0 ± 0.3
9	0.028	4.2	8 ± 3	-1.0 ± 0.3
10	0.027	5.2	7 ± 2	-1.0 ± 0.3
11	0.033	2.1	5 ± 3	-1.0 ± 0.3

3.2 Hess diagrams

Hess diagrams have played an increasingly prominent role in the analysis of photometric data, in particular of the Magellanic Clouds. They show the frequency or density of occurrence of stars at various positions on the CMD, thus providing a star density map in the CMD. Hess diagrams have been profitably exploited by using different robust techniques (Harris & Zaritsky 2001; Dolphin 2002, and references therein). Here, we simply take advantage of Hess diagrams to identify the prevailing features – in terms of density of stars – and their intrinsic dispersions in the cleaned SMC CMDs. In order to produce these Hess diagrams we counted the number of stars placed in different magnitude–colour bins with sizes $[\Delta T_1, \Delta(C-T_1)] = (0.1, 0.05)$ mag and then we represented the resultant count scales with a 10-grey-level logarithmic scale. The resultant Hess diagrams for the observed and cleaned SMC CMDs are depicted in a series of panels in Fig. 4.

The cleaned Hess diagrams exhibit different features which tell us about the stellar populations in the surveyed SMC region. A mixture of intermediate-age through old stellar populations clearly appears to be the main feature of these Hess diagrams. Since the SMC field CMDs are obviously composed of stars of different stellar populations, the respective Hess diagrams allow us to recognize the so-called dominant populations (generally darker regions in the Hess diagrams). These stellar populations are the most numerous in a particular region and can be referred as the 'representative' stellar population along the line of sight (LOS) of that SMC field (P12, Piatti & Geisler 2013; Piatti et al. 2014a). The definition of a representative population could not converge to any dominant population if the stars in a given field came from a constant SFR integrated overall time. For our fields, however, we could clearly identify the respective most populated features. Particularly, the representative MSTOs are in average ∼1.5 mag brighter than the T_1 magnitudes for the 100 per cent completeness level of the respective field, i.e. the faintest T_1 magnitude where completeness is still 100 per cent. Therefore, we actually reach the MSTO of the representative population of each field with a negligible loss of stars at that magnitude.

The most distant MS populations from the SMC centre detected by our photometry are located at an angular distance of ∼5°.7 (Field 7), equivalent to 6.1 kpc if the SMC distance modulus of 18.96 mag is adopted (de Grijs & Bono 2015). The adopted optical SMC centre is $00^h52^m45^s$, $-72°49'43''$ (J2000) (Crowl et al. 2001). We did not find any visible sign of farther clear SMC MS other than the residuals from the MW/background contamination. The resulting SMC radius is in very good agreement with those

obtained by Noël & Gallart (2007, ∼6.3 kpc) from *BV* photometry of three SMC fields and by De Propris et al. (2010, ∼6 kpc) from Ca ɪɪ triplet spectroscopy of giant stars, among others. However, it results shorter than the SMC peripheral boundary estimated by Nidever et al. (2011, ∼10.7 kpc). Their data cover a much larger area of the SMC, which allowed them from the analysis of the giant stellar component to find evidence for a break population beyond ∼8 kpc with a shallow radial density profile that could be either a bound stellar halo or a population of extratidal stars. In this context, our results confirm that the bulk of the SMC population is contained within ∼7° from the galaxy centre, independently of any possible dependence of the SMC extent with the position angle, beyond which there is a low-density envelope extending further out found by Nidever et al. (2011). Note additionally that some previous studies have suggested the existence of different asymmetries in the SMC (e.g. Subramanian & Subramaniam 2012; Cignoni et al. 2013; Rubele et al. 2015). Nevertheless, we also carried out counts of red giant clump stars within the box $(\Delta(C-T_1),\Delta(T_1)) = (0.95–1.70, 17.90–19.70)$ in the cleaned and observed CMDs. The results are depicted in Fig. 5, where we added a constant to the counts in the cleaned CMDs for comparison purposes and indicated the count level for the outermost field Field 1 (at 12°.8, equivalent to 13.8 kpc) with a horizontal line. The uncertainties introduced by both the errors in the relative SMC field reddening and in the photometry are much smaller than the symbol size. The similar shape of both profiles tell us about the robustness of the cleaning procedure, since a similar number of stars was subtracted from each field, once they were properly corrected by incompleteness and reddening effects. On the other hand, the profiles show that the SMC red clump star population that our analysis is able to detect would not appear to extend beyond ∼6°–7° (∼6.6–7.7 kpc).

4 ANALYSIS

We used the cleaned CMDs and Hess diagrams of Fields 7–11 to constrain the fundamental SMC field parameters by matching the observations with the theoretical isochrones of Bressan et al. (2012) and by using the new age–metallicity diagnostic diagram for the Washington photometric system (Piatti & Perren 2015).

The estimation of the mean SMC field reddening values was made by taking advantage of the NASA/IPAC Extragalactic Data base[5] (NED) to obtained Galactic foreground reddening values for the SMC field list. We adopted the recent recommendation for the mean SMC distance modulus $(m-M)_0 = 18.96$ mag, whose formal uncertainty is 0.02 mag but can reach 0.15–0.20 mag if the complex SMC geometry is particularly considered (de Grijs & Bono 2015). Bearing in mind a 1σ LOS depth of 6 kpc (Deb et al. 2015), we found that the difference in apparent distance moduli could be as large as $\Delta(T_1 - M_{T_1}) \sim 0.2$ mag. This difference is smaller than the difference between two closely spaced isochrones as used here $(\Delta \log(t \, yr^{-1}) = 0.1, \Delta(M_{T_1}$ at the MSTO-subgiant branch region) ∼0.3 mag), so that adoption of a unique value for the distance modulus does not dominate the final error budget incurred in matching isochrones to the SMC field Hess diagrams.

We used the ridge lines of the representative SMC field MSs in the Hess diagrams (darker places) to properly find the theoretical isochrones which best superimpose on them. As for the metallicity, we used the values derived from the new age–metallicity diagnostic

---

[5] http://ned.ipac.caltech.edu/. NED is operated by the Jet Propulsion Laboratory, California Institute of Technology, under contract with NASA.
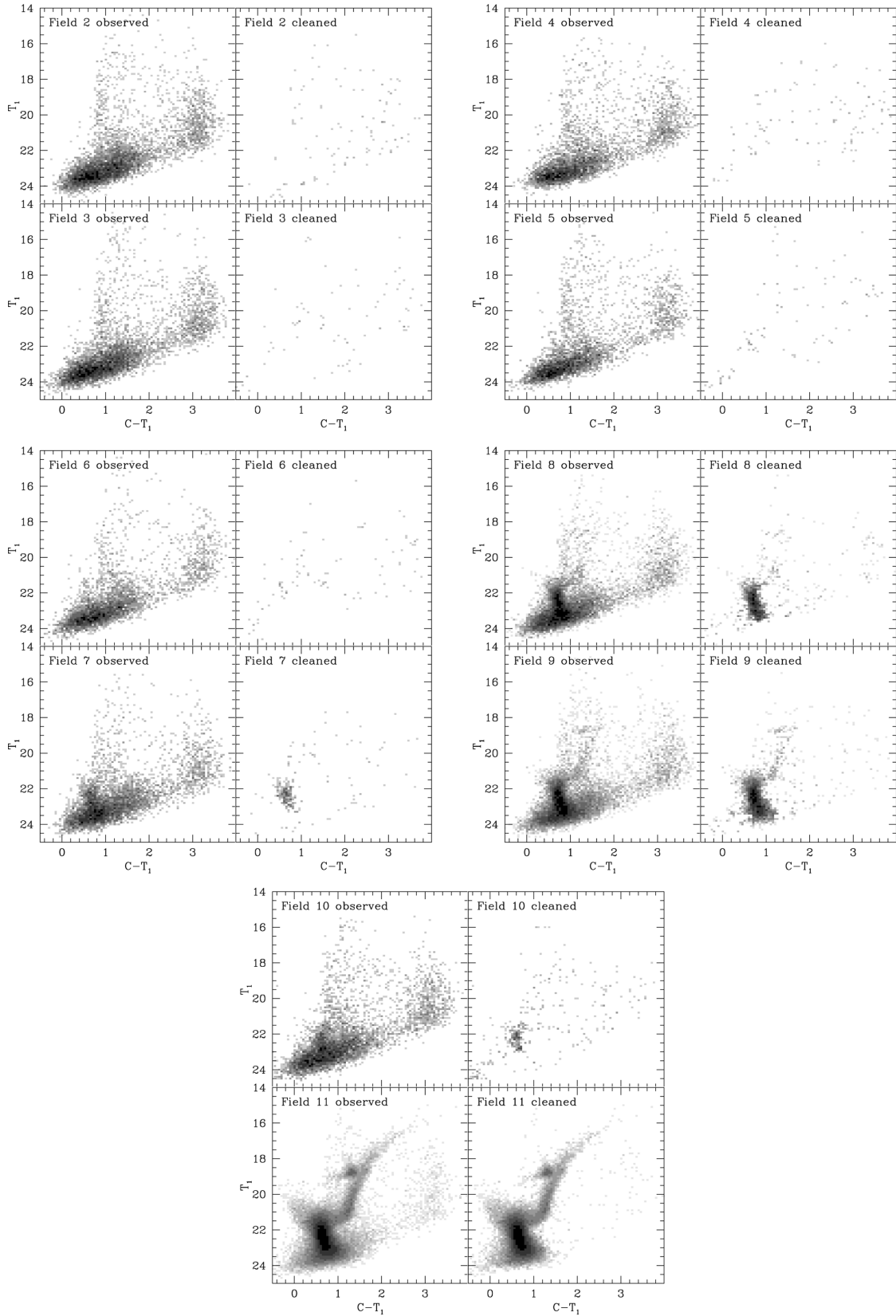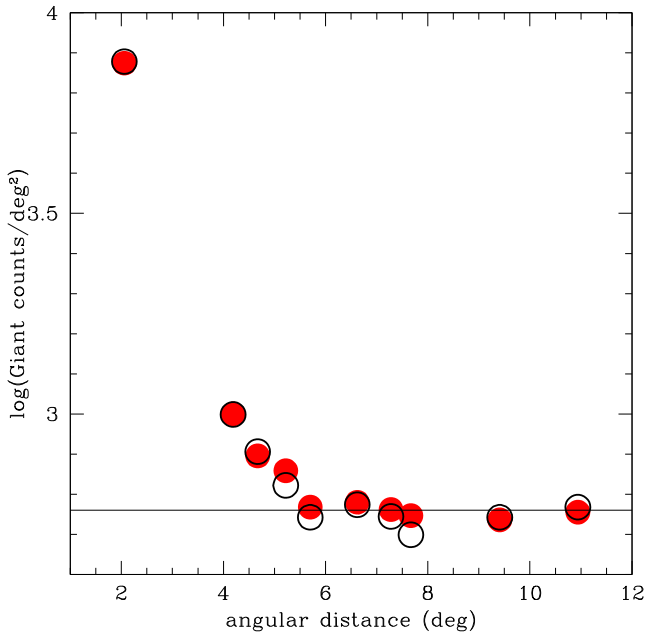
**Figure 4.** Observed and field star-decontaminated Hess diagrams.

Figure 5. Counts of red giant clump stars within the box $(\Delta(C - T_1), \Delta(T_1))$ = (0.95–1.70, 17.90–19.70) in the cleaned (red circle) and observed (open circle) CMDs of the studied SMC fields in terms of their angular distances to the SMC centre. The former have been shifted by a constant for comparison purposes. The horizontal line represents the counts level for the outermost studied field (Field 1).

diagram based on the magnitude difference between the red giant clump and the MSTO (Piatti & Perren 2015, see their fig. 4). We assigned the age of such isochrones to the representative ages of each SMC field. Table 3 lists the derived representative ages and metallicities and their dispersions. The age dispersions have been estimated bearing in mind the broadness in magnitude and colour of the dominant MSs, which represent in general a satisfactory estimate of the age spread around the prevailing population. The metallicity dispersions come from the estimated spread in magnitude of the red clump and the MSTO. Fig. 6 depicts the cleaned Hess diagrams with three different theoretical isochrones superimposed for comparison purposes.

The derived representative ages and metallicities suggest a constant metallicity level ([Fe/H]= −1.0 dex) and an approximately constant age value (≈7–8 Gyr) for the western SMC periphery. We plot these values in Fig. 7 with solid circles, whereas we represent their dispersions with error bars. Note that the youngest age (5 Gyr) corresponds to Field 11, which is located within the SMC main body. Similar age/metallicity values were found by Carrera et al. (2008) from Ca ɪɪ triplet spectroscopy of giants in four fields located towards the western side of the SMC main body, as well as by Noël et al. (2009) who studied 12 SMC star fields from *BR* photometry (see Fig. 7). The present AMR does not clearly differ from that obtained by P12 for the SMC main body using the same techniques, reproduced by open circles in Fig. 7. The mean SMC AMR derived by P12 is in overall very good agreement with those obtained by Cignoni et al. (2013, see their fig. 14 and discussions therein), Rubele et al. (2015, see their fig. 17 and discussions therein), among others.

We did not find in the western SMC periphery dominant stellar populations older than ∼10 Gyr, but a peak centred at ∼7–8 Gyr. This peak is in excellent agreement with the SFRs recovered by Carrera et al. (2008), Noël et al. (2009), Cignoni et al. (2013), and
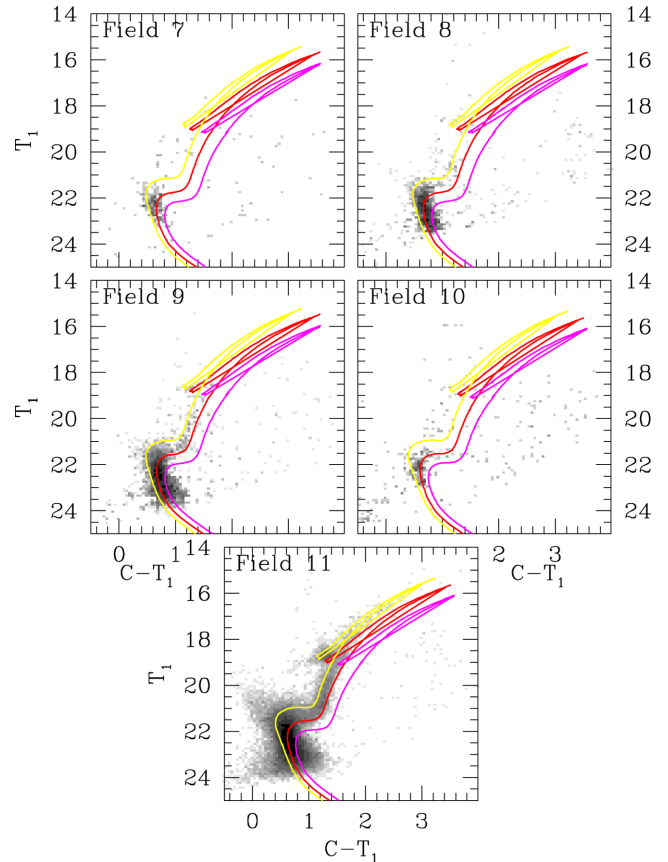
Figure 6. Hess diagrams for studied fields with SMC signatures. Three theoretical isochrones taken from Bressan et al. (2012) were superimposed as reference of the dominant ages and metallicities: magenta, red, and yellow lines correspond to (age, [Fe/H]) = (5 Gyr, −1.3 dex), (8 Gyr, −1.0 dex) and (10 Gyr, −0.7 dex), respectively, for Field 7, 8, and 9, and (age, [Fe/H]) = (4 Gyr, −1.3 dex), (6.3 Gyr, −1.0 dex) and (8 Gyr, −0.7 dex), respectively, for Field 10 and 11.

Rubele et al. (2015, see their fig. 16), who also showed a low initial SFR at ∼10 Gyr. Particularly, Rubele et al. (2015) showed that the stellar mass formation – measured as the relative to the total galaxy–mass ratio – reached a peak ∼8 Gyr ago. In this context, it seems that the western SMC periphery does not distinguish itself from the major formation processes that took place during the galaxy formation epoch.

5 CONCLUSIONS

We have studied the western SMC periphery from Washington CT_1 photometry of 11 star fields (36×36 arcmin^2 each) covering angular distances to the SMC centre from 2° up to ∼13° (≈2.2–13.8 kpc). Our photometric data base reaches the 50 per cent completeness level ∼2–3 mag below the oldest SMC MSTOs, depending on the crowding.

We cleaned the noticeable MW/background field contamination present in the observed SMC star field CMDs using a procedure which makes use of boxes of variable side centred on every star in the MW/background CMD, in order to tightly reproduce it in terms of stellar density, luminosity function, and colour distribution. We subtracted the stars in the SMC CMDs that fall within the defined boxes and are closest to the defined box centres.
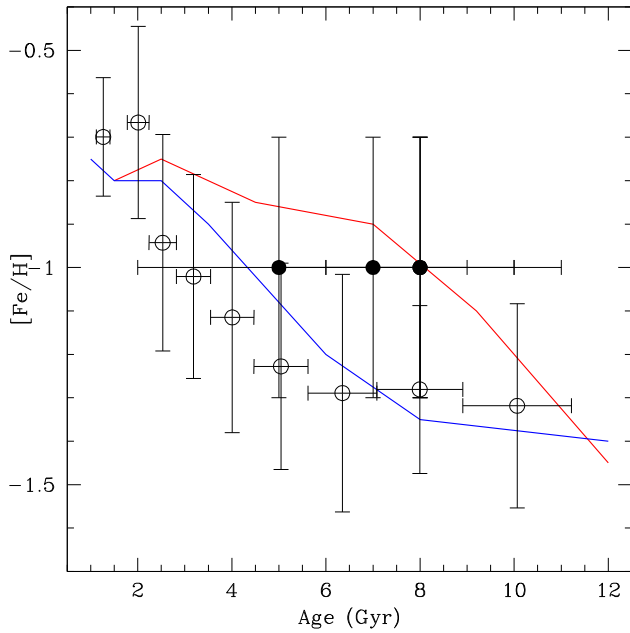
Figure 7. AMR for the presently studied SMC star fields (solid circles), with the dispersion in age and in metallicity represented by error bars. The mean AMRs by Carrera et al. (2008, red line), Noël et al. (2009, blue line), and Piatti & Geisler (2013, open circles with error bars) are overplotted.

From the cleaned CMDs (and hence the respective Hess diagrams) we identified the representative (most numerous) stellar populations of each field. Particularly, the most distant representative MS populations from the SMC centre detected by our photometry are located at an angular distance of ∼5°7 (6.1 kpc); no sign of farther SMC MS stars is visible other than the residuals from the MW contamination.

The derived representative ages and metallicities suggest a constant metallicity level ([Fe/H] = −1.0 dex) and an approximately constant age (≈7–8 Gyr) for the composite stellar population of the western SMC periphery. These values do not clearly differ from those of the most comprehensive AMRs derived for almost the entire SMC main body.

Finally, the range of ages of the representative stellar populations in the western SMC periphery confirm previous results about the major star formation processes from which the galaxy was born. Indeed, after a low SFR at ∼10 Gyr, the SMC experienced its first significant star formation activity period which peaked ∼7–8 Gyr ago.

ACKNOWLEDGEMENTS

REFERENCES

Balbinot E. et al., 2015, MNRAS, 449, 1129
Bica E., Bonatto C., Dutra C. M., Santos J. F. C., 2008, MNRAS, 389, 678
Bressan A., Marigo P., Girardi L., Salasnich B., Dal Cero C., Rubele S., Nanni A., 2012, MNRAS, 427, 127
Canterna R., 1976, AJ, 81, 228
Carrera R., Gallart C., Aparicio A., Costa E., Méndez R. A., Noël N. E. D., 2008, AJ, 136, 1039
Cignoni M., Cole A. A., Tosi M., Gallagher J. S., Sabbi E., Anderson J., Grebel E. K., Nota A., 2013, ApJ, 775, 83
Crowl H. H., Sarajedini A., Piatti A. E., Geisler D., Bica E., Clariá J. J., Santos J. F. C., Jr, 2001, AJ, 122, 220
de Grijs R., Bono G., 2015, AJ, 149, 179
De Propris R., Rich R. M., Mallery R. C., Howard C. D., 2010, ApJ, 714, L249
Deb S., Singh H. P., Kumar S., Kanbur S. M., 2015, MNRAS, 449, 2768
Dolphin A. E., 2002, MNRAS, 332, 91
Geisler D., 1996, AJ, 111, 480
Harris J., Zaritsky D., 2001, ApJS, 136, 25
Jannuzi B. T., Claver J., Valdes F., 2003, The NOAO Deep Wide Field Survey MOSAIC Data Reductions. Available at: http://www.noao.edu/noao/noaodeep/ReductionOpt/frames.html
Maia F. F. S., Piatti A. E., Santos J. F. C., 2014, MNRAS, 437, 2005
Nidever D. L., Majewski S. R., Muñoz R. R., Beaton R. L., Patterson R. J., Kunkel W. E., 2011, ApJ, 733, L10
Noël N. E. D., Gallart C., 2007, ApJ, 665, L23
Noël N. E. D., Aparicio A., Gallart C., Hidalgo S. L., Costa E., Méndez R. A., 2009, ApJ, 705, 1260
Piatti A. E., 2011a, MNRAS, 416, L89
Piatti A. E., 2011b, MNRAS, 418, L40
Piatti A. E., 2011c, MNRAS, 418, L69
Piatti A. E., 2012a, MNRAS, 422, 1109 (P12)
Piatti A. E., 2012b, A&A, 540, A58
Piatti A. E., 2014, MNRAS, 440, 3091
Piatti A. E., Bica E., 2012, MNRAS, 425, 3085
Piatti A. E., Geisler D., 2013, AJ, 145, 17
Piatti A. E., Perren R., 2015, MNRAS, 450, 3771
Piatti A. E., Geisler D., Mateluna R., 2012, AJ, 144, 100
Piatti A. E., del Pino A., Aparicio A., Hidalgo S. L., 2014a, MNRAS, 443, 1748
Piatti A. E. et al., 2014b, A&A, 570, A74
Piatti A. E., de Grijs R., Rubele S., Cioni M. R., Ripepi V., Kerber L., 2015, MNRAS, 450, 552
Robin A. C., Reylé C., Derrière S., Picaud S., 2003, A&A, 409, 523
Roderick T. A., Jerjen H., Mackey A. D., Da Costa G. S., 2015, ApJ, 804, 134
Rubele S. et al., 2015, MNRAS, 449, 639
Stetson P. B., Davis L. E., Crabtree D. R., 1990, in Jacoby G. H., ed., ASP Conf. Ser. Vol. 8, CCDs in Astronomy. Astron. Soc. Pac., San Francisco, p. 289
Subramanian S., Subramaniam A., 2012, ApJ, 744, 128
Weisz D. R., Dolphin A. E., Skillman E. D., Holtzman J., Dalcanton J. J., Cole A. A., Neary K., 2013, MNRAS, 431, 364

SUPPORTING INFORMATION

Additional Supporting Information may be found in the online version of this article:

Table 2. CT_1 data of stars in Field 1 (http://mnras.oxfordjournals.org/lookup/suppl/doi:10.1093/mnras/stv1179/-/DC1).

Please note: Oxford University Press are not responsible for the content or functionality of any supporting materials supplied by the authors. Any queries (other than missing material) should be directed to the corresponding author for the article.

This paper has been typeset from a TEX/LATEX file prepared by the author.